Mapping Floods due to Hurricane Sandy from the NPP VIIRS and ATMS data

Donglian Sun[1], Sanmei Li[1], Wei Zheng[1], Arie Croitoru[1], Anthony Stefanidis[1], and Mitchell Goldberg[2]

[1]Department of Geography and Geoinformation Science
George Mason University
[2]NOAA JPSS Program Office, Lanham, MD 20706

Abstract

In this study, we present an approach to estimate the extent of large-scale coastal floods caused by Hurricane Sandy using passive optical and microwave remote sensing data. The approach estimates the water fraction from coarse-resolution VIIRS and ATMS data through mixed-pixel linear decomposition. Based on the water fraction difference, using the physical characteristics of water inundation in a basin, the flood map derived from the coarse-resolution VIIRS and ATMS measurements was extrapolated to a higher spatial resolution of 30 meters using topographic information. It is found that flood map derived from VIIRS shows less inundated area than the FEMA flood map and the ground observations. The bias was mainly caused by the time difference in observations. This is because VIIRS can only detect flood under clear conditions, while we can only find some clear sky data around the New York area on Nov. 4th, 2012, when most flooding water already receded. Meanwhile, microwave measurements can penetrate clouds and sense surface water under clear-or-cloudy conditions. We therefore developed a new method to derive flood maps from passive microwave ATMS observations. To evaluate the flood mapping method, the corresponding ground observations and the FEMA storm surge flooding (SSF) product are used. The results show there was good agreement between our ATMS and the FEMA SSF flood areas, with a correlation of 0.95. When evaluated against ground observations from the social-media data, it is found that 95% of the flickr flood reports

were distributed within the ATMS-derived flood area. Overall, the proposed methodology was able to produce high-quality and high-resolution flood maps over large-scale coastal areas.

Key Words: Coastal flood, Hurricane, Water fraction, High-resolution flood mapping, VIIRS, and ATMS.

1. Introduction

Hurricane Sandy, the largest Atlantic hurricane on record, devastated portions of the Mid-Atlantic and Northeastern United States in late October 2012. Preliminary estimates of losses that include business interruption surpass $50 billion (2012 USD).

Rapid assessment of the spatial extent of large-scale flooding event is highly important for relief and rescue operations, and satellite remote sensing is eminently appropriate for this task (Sheng et al. 2001, Sun et al. 2011, 2012). Under clear conditions during the daytime, flood maps can be derived from optical sensors, such as visible (VIS), near-infrared (NIR) (Sheng et al. 2001, Sun et al. 2011, 2012), and shortwave-infrared (SWIR) observations (Li et al. 2012). Compared with optical remote sensing instruments, microwave sensors, including active airborne synthetic aperture radar (SAR) imagery (Battes et al. 2006), and passive microwave instruments (Sippel et al. 1994, Jin 1999, Tanaka et al. 2003, Zheng et al. 2008) can penetrate through clouds and sense surface water bodies. Compared with active microwave sensors, passive microwave instruments can provide observations at higher temporal resolutions; therefore, these data have great potential for estimating large-scale floods, particularly under cloudy conditions that are typically associated with floods. However, the coarse spatial resolution of passive microwave sensors may limit their broad application.

In this study, flooding due to Hurricane Sandy was derived from the NPP VIIRS 375-m imager data and microwave ATMS data, and enhanced to a 30-m resolution using the SRTM DEM data. The results show good agreement with the FEMA flood map and ground observations.

2. Data Used

To estimate the coastal flooding due to Sandy, the data used are listed as follows:

1) The NPP VIIRS data (Table 1) were obtained from NOAA's Comprehensive Large Array-Data Stewardship Systems (CLASS).
2) The ATMS antenna temperature data records (TDR) were obtained from NOAA's CLASS (Weng et al. 2013). Brightness temperatures and satellite zenith angles were extracted from the ATMS HDF5 files. These data were then re-projected into the WGS84 system and re-sampled to 15km x 15km spatial resolution. The channels shown in Table 2 can be used to observe the earth's surface.
3) Digital elevation model (DEM) data from Shuttle Radar Topography Mission (SRTM).
4) River basin boundary data, distributed by the US Geological Survey (USGS), were used to obtain water fraction statistics for high-resolution flood mapping. To construct the mixed pixels along the coastline, the coastline on the river basin boundary was buffered toward the ocean.
5) Land cover data, acquired from the National Land Cover Database (NLCD) 2006 of USGS, are used to obtain pure end-member data and to extract background water information.
6) Linear hydrographic features (major rivers, streams, and canals) and area hydrographic

features (major lakes and reservoirs) were used for estimating river density and for deriving pure land end-member data.

7) Three-meter-resolution Hurricane Sandy SSF products generated from field-verified High-Water-Marks (HWM) and Storm Surge Sensor data and distributed by the Federal Emergency Management Agency (FEMA) were used to evaluate the ATMS-derived flood map. The SSF products were created from the HWMs and storm surge sensor data from the USGS. The HWMs and surge sensor data are used to interpolate the water surface elevation; then, the water elevation data are subtracted from the best available DEM to create a depth grid and surge boundary.

8) Ground-level observations from open-source social media content, namely, geolocated flickr imagery that reported flooding, as an additional dataset to evaluate the satellite-derived flood map.

3. Methodology

3.1. Derive Flooding Water Fraction from VIIRS under Clear Conditions

Under clear sky conditions, a decision tree algorithm will be applied to identify flooded areas (Sun et al. 2011, 2012, Li et al. 2012). Since flood is land inundated by water, flooded pixels are usually water mixed with land. As such, only water fraction can represent this mixed information, so flood map derived from water fraction contains more information than that derived from water classification (Sun et al. 2011). Water fraction can be calculated from linear mixture model and a dynamic nearest neighbor searching (DNNS) method developed by Li et al. (2012):

$$f_w = \frac{R_{ch\_land} - R_{ch\_mix}}{R_{ch\_land} - R_{ch\_water}} \quad (1)$$

By using the characteristic of the VIIRS visible channel I1 (ch1:0.64 μm), near IR channel I2 (ch2: 0.865 μm) and Shortwave IR (SWIR) channel I3 (ch3: 1.61 μm), the DNNS method can be used to dynamically search the nearby land and water end members:

$$\frac{R_{ch1\_mix}}{R_{ch3\_mix}} - \frac{R_{ch1\_water}}{R_{ch3\_mix}} < \frac{R_{ch1\_land}}{R_{ch3\_land}} < \frac{R_{ch1\_mix}}{R_{ch3\_mix}}$$

$$\frac{R_{ch2\_mix}}{R_{ch3\_mix}} - \frac{R_{ch2\_water}}{R_{ch3\_mix}} < \frac{R_{ch2\_land}}{R_{ch3\_land}} < \frac{R_{ch2\_mix}}{R_{ch3\_mix}} \quad (2)$$

Flooding water fraction can be obtained by the difference in water fraction after and before flood.

3.2. Cloud Shadow Detection

Another critical component of this technique is a geometric correction method recently developed by Li et al. (2013a) to remove cloud shadows from water detection results (Li et al. 2013a). This is a critical step in flood mapping, as current techniques that rely on optical satellite imagery are severely affected by a large portion of cloud shadow pixels that are misclassified as water. The viability of necessary retrieval methods and new sensor capabilities has been demonstrated for flood detection using Hurricane Sandy, and the recent flood cases in Alaska and Colorado as primary operational test scenarios. The flowchart for deriving water fraction and flood from VIIRS is described in Figure 1.

3.3. Inundation Model to Derive High Resolution Flood Maps

According to water's hydrodynamic properties, when flooding occurs, inundated areas are affected sequentially from lowest to the highest point in elevation. If the topography is not very steep around the water bodies, the higher the water level, the larger the inundated area. This inundation mechanism can be expressed as:

$$\mathrm{A} = \int_{\min\_h}^{\max\_h} f(h)dh \qquad (3)$$

where, A is the total water area between the minimal surface elevation, $\min\_h$, and maximal inundated surface elevation, $\max\_h$; and $f(h)$ is the increment of water area with the change of surface elevation h. Equation (3) indicates the relationship between inundated area and surface elevation. Because both the minimal surface elevation, $\min\_h$, and the increment function of water area in a specific region, $f(h)$,can be derived from the digital elevation model (DEM), the maximal inundated surface elevation, $\max\_h$, decides the total water area (Li et al. 2013b). Consequently, the maximal inundated surface elevation, $\max\_h$, can also be calculated if the total water area A is known.

Since optical satellite data, such as VIIRS, can only map the land surface under clear-sky conditions when major locations affected by Sandy can only be detected four days after the hurricane's passing (November 4, 2012). As shown in Figure 4, by that time, flooding conditions had already receded in most affected regions. The peak floods due to Hurricane Sandy were under cloudy conditions. Accordingly, we developed a new algorithm to derive flood maps from passive microwave data; namely, the ATMS sensor on board the Suomi-NPP, which can penetrate through clouds to observe the surface.

3.4. Derive Flooding Water Fraction from ATMS under All Weather Conditions

3.4.1. Precipitating cloud detection

Despite its overall resilience in cloudy conditions, passive microwave signals can still be affected by clouds (Cho and Nishiura 2010). In particular, higher frequency channels cannot penetrate precipitating clouds. Before extracting the surface information, precipitating clouds should be detected and masked. Precipitating clouds can be defined by comparing the brightness temperature at 89 GHz versus 22 GHz, as the former has substantially lower values (Ferraro et al. 1998). Accordingly, we defined a pixel in the ATMS imagery as a cloud-contaminated pixel if it met the following condition:

$$BT_{16} - BT_{1} < T_{\text{RAIN}} \tag{4}$$

where BT_{16} and BT_{1} are the brightness temperatures of channels 16 and 1, respectively, and T_{RAIN} (10.0) is a threshold value to distinguish precipitation areas from other objects.

3.4.2. Satellite zenith angle limitation

Pixels with large satellite zenith angles have a lower spatial resolution than those near nadir. Accordingly, we chose the pixels with smaller angles to extract related information by removing pixels with satellite zenith angle greater than 50º. Satellite zenith angle data are available in ATMS's HDF5 file, which provides such information for each ATMS pixel.

3.4.3. Water fraction calculation method

Water body detection and area calculations are key steps for flood estimations. Channels 3 and 4 of the ATMS data have longer wavelengths and better penetrate clouds than channel 16. Furthermore, these two channels are similarly affected by the atmosphere due to their similar frequencies. Following previous researchers' use of the polarization difference of 37 GHz (Sippel et al. 1994, Choudhury 1989, Sippel et al. 1998), in this study, the brightness temperature difference ($\Delta T_{(4\text{-}3)obs}$) between channels 4 and 3 was used to identify water and land. To test the sensitivity of $\Delta T_{(4\text{-}3)obs}$ to water and land, land and water samples were selected from the ATMS data on October 16, 17, 21, 22, 26, 27 and November 1 according to the land cover.

The spatial resolution of ATMS data is 15 km. At this coarse resolution, the land surface is generally comprised by mixed terrain of water and land. ATMS pixels consist of a combination of different microwave signals generated by the water and the land surface fractions, and can be represented as following:

$$\Delta T_{(4\text{-}3)obs} = f_{wat}\Delta T_{(4\text{-}3)wat} + f_{lan}\Delta T_{(4\text{-}3)lan} \tag{5}$$

$$1 = f_{wat} + f_{lan} \tag{6}$$

where, $\Delta T_{(4\text{-}3)obs}$ is the brightness temperature difference of ATMS channels 3 and 4. $\Delta T_{(4\text{-}3)wat}$ and $\Delta T_{(4\text{-}3)lan}$ are the brightness temperature difference of channels 3 and 4 for water and land, respectively. f_{wat} and f_{lan} represent the fractions of water and land, respectively. According to equations 5 and 6, we can get:

$$\Delta T_{(4-3)obs} = f_{wat}\Delta T_{(4-3)wat} + (1 - f_{wat})\Delta T_{(4-3)lan} \tag{7}$$

$$\Delta T_{(4-3)obs} = f_{wat}(\Delta T_{(4-3)wat} - \Delta T_{(4-3)lan}) + \Delta T_{(4-3)lan} \tag{7'}$$

From equation 7, water fraction f_{wat} can be derived from the following equation:

$$f_{wat} = \frac{\Delta T_{(4\text{-}3)obs} - \Delta T_{(4\text{-}3)lan}}{\Delta T_{(4\text{-}3)wat} - \Delta T_{(4\text{-}3)lan}} \tag{8}$$

Two end elements need to be calibrated: $\Delta T_{(4\text{-}3)lan}$ and $\Delta T_{(4\text{-}3)wat}$. The calibration of the $\Delta T_{(4\text{-}3)wat}$ is rather straightforward, as it can be derived by analyzing the brightness temperatures measured over the lakes or ocean. $\Delta T_{(4\text{-}3)lan}$ is calibrated over some selected pixels, which are chosen based on the ATMS channel characters, DEM data, and river basin boundary data. The calibration of land pixels is more complicated, because land end members are related to soil moisture, vegetation, and soil types, and other physiognomical factors.

To find the pure end-member more accurately, we built pure land sample regions according to the land cover data and river density information. We selected land sample pixels with both low river density and similar land cover types to the coastland. Ocean pixels near the coastline were selected as water sample regions. The flowchart for deriving water fraction from ATMS is shown in Figure 2.

4. Results

4.1. Derive high resolution flood map from VIIRS

Figure 3 (left) shows a false-color image of the VIIRS instrument over the New York metropolitan area, while Figure 3 (upper) shows the derived water fraction distribution in the same area on Nov. 04, 2012.

With the water detection result, floodplains can be determined by subtracting water extent before flood. For operational products, we can use water reference map from MODIS Water Mask Product (MOD44W) (Carroll et al., 2009) or generate a dynamic reference water map from a composite of water identification map in all clear days during previous month. However, with the original spatial resolution 375 m of VIIRS, as shown in Figure 3, the flooded area in small regions, like New York, during Hurricane Sandy period, can't be detected. By applying an inundation model recently developed by Li et al. (2013a) and ingesting DEM data from the SRTM, flood maps derived from VIIRS can be upgraded to 30 m resolution.

Figure 4 shows a flood map around the New York metropolitan area derived from VIIRS and SRTM 30-m DEM data on Nov. 04, 2012, when only some clear sky data around the New York area can be found. Compared with flooding zone maps from the FEMA and evacuation estimates during Hurricane Sandy, the VIIRS 30-m flood map on Nov. 4^{th}, 2012 shows consistent inundated locations. Nevertheless, the flood map derived from VIIRS shows less inundated area than the FEMA flood map and the ground observations. This is because most flooding water due to Sandy already receded on Nov. 4^{th}, 2012.

4.2. Derive high resolution flood map from ATMS

Since microwave instruments, like Radar and ATMS, can penetrate through clouds to observe the Earth surface, but the Radar data is usually very expensive, we therefore developed a new method to derive flood maps from passive microwave ATMS observations.

The water fraction of each ATMS pixel was estimated in accordance with the principle of linear decomposition of mixed pixels. The land and water samples regions generated by river density and land cover data, the relationship of channels 3, 4 and 16, neighborhood pixels searching, and the difference of channels 4 and 3 of ATMS were comprehensively taken into account to dynamically decide the water and land endmembers.

Figure 5 shows the resulting water fraction maps derived from the ATMS before and after Hurricane Sandy. With the water detection result at the ATMS coarse resolution (15km), floodplains can be determined by subtracting water extent before flood. The basin-scale water fraction differences between before and after the flood were calculated to derive flood map, and to reduce the affection of soil moisture and vegetation, avoiding the pixel-to-pixel errors. Figure 3 (c) demonstrates the flood map derived from the ATMS.

However, the spatial resolution from passive microwave sensor is usually very coarse (e.g. 15 km for the ATMS). The primary limitation of ATMS data for flood detection is its coarse spatial resolution (15 km^2). It is difficult to obtain detailed information about the flood distribution from the original water fraction results because of the coarse resolution. According to the characters of water distribution in a basin, combining with high resolution DEM data, high-resolution flood mapping can be obtained using the inundation model recently developed by Li et al. (2013c). By applying this inundation model and the DEM derived from the 30m SRTM observations, water fraction and flood map derived from the ATMS can be enhanced to fine 30 m resolution. Figure 6 (upper) shows the flood map at 30 m resolution derived from the SRTM DEM data with the inundation model.

4.3. Evaluations

4.3.1. Comparison to a similar flood map produced by FEMA

Compared with the flooding map derived from the VIIRS as shown in Figure 4, the ATMS 30-m flood map on Nov. 1st, 2012 shows consistent inundated locations with the flood zone maps from FEMA (Figure 4 Lower). We further make a quantitative comparison to the SSF products distributed by FEMA (http://fema.maps.arcgis.com/home/index.html) during the Hurricane Sandy period. The SSF product, i.e., the flood information distributed by FEMA during Hurricane Sandy, included the states of NJ (New Jersey), NY (New York), and CT (Connecticut) (Figure 6). For quantitative evaluation, the SSF product was re-sampled from 3 m to the same 30-m resolution and overlapped with our ATMS-derived flood map. The flood map derived from the ATMS and DEM data shows even more inundated area than the FEMA SSF product. Further quantitative assessment indicates a good agreement between the ATMS-derived and the FEMA SSF flood map (Figure 6) with correlation 0.95. One of the main sources for the remaining inconsistency or errors may be due to spatial resolution differences of the various datasets. Although we re-sampled all the datasets to the same 30-m spatial resolution, slight displacements of ATMS would cause a substantial shift in our ATMS-derived product, as it is compared with the fine 3-meter resolution of the SSF product. Differences in the scope between ATMS-derived flood map and the SSF products can also be reasonably expected, because inland water inundation caused by hurricane-associated precipitation was not connected with the coastline or ocean. This type of flooding was reflected by microwave ATMS signal, but was not included in the SSF products; thus, differences were observed when the two datasets were compared.

4.3.2. Evaluation against ground-level observations from social-media flood reports

In a next step, we compared our map to crowdsourced data from social media. The emergence of social media has provided another avenue for event reporting, with citizens contributing real-time information about breaking news. The popularity of platforms such as Twitter and YouTube and the substantial amount of content that is communicated through them are making social media a powerful open-source addition to authoritative datasets (Stefanidis et al. 2013). The information communicated through such feeds is often geolocated, and the analysis of this geospatial content may lead to the identification of patterns that can be correlated to physical events.

For this particular application, we focused on flickr imagery. We collected all geolocated flickr imagery that reported flooding in our study area within one week after the hurricane, and we compared these data to our ATMS-derived flood map. We collected flickr data through flickr's publicly accessible application programming interface (API). The flickr data are images uploaded to the social media website over a week-long period starting on October 30, 2012, that explicitly mention the words 'flood' and 'Sandy' in their descriptions. A total of 1,059 geolocated images were obtained. In Figure 7, we see the spatial coincidence between these two datasets. It is found that 95% of the flickr flood reports were distributed within the ATMS-derived flood area. We proceeded with the flickr data in this case, rather than twitter, because twitter traffic was saturated with references to flooding even from locations that were not affected by it. The flickr imagery was reasonably assumed to represent locations inside or adjacent to the flood zone (see Figure 7). The significance of this finding is twofold. First, it offers a further argument for the quality of the ATMS-derived flood map. Second, one could argue, more importantly, that this study presents a comparison of the spatial distribution of flickr imagery that report a flood event relative to the event itself at a large scale. The ground-level imagery that we used in this study were not contributed as a response to a specific request for data, but rather it was information contributed directly to flickr by the general public as part of its normal social media activities. Therefore, it presents an unbiased representative example of social media content as it relates to flooding events. Accordingly, we argue that our results offer a first real-data-based, large-scale-study argument in support of the high potential of using crowdsourced information (flickr, here).

4. Summary and Discussions

The high temporal resolution and large coverage of coarse- to moderate-resolution satellite imagery, such as VIIRS and ATMS onboard the NPP and future JPSS, are very advantageous for flood monitoring, but their coarse spatial resolution limits their wider application. Overcoming this limitation is an interesting scientific challenge with substantial application potential.

In this study, VIIRS observations are used to estimate floods induced by Hurricane Sandy along a coastline and New York area in late October and early November of 2012. But with the original resolutions, floods in small region cannot be identified, we therefore applied a recently developed inundation model to upscale VIIRS 375-m water fraction and flood maps to 30-m resolution by using the SRTM 30-m DEM data. It is found that flood map derived from VIIRS data shows less inundated area than the FEMA flood map and the ground observations. This is because optical sensor can only observe the Earth surface under clear-sky conditions, while clear data can only be found four days after the hurricane's passing on November 4, 2012, when major floods due to Hurricane Sandy already receded. The peak floods were associated with cloudy conditions. Since microwave instruments, like Radar and ATMS, can penetrate through clouds to watch the Earth surface, but the Radar data is usually very expensive, we therefore developed a new method to derive flood maps from passive microwave ATMS observations. The flood map derived from the ATMS is also improved to 30-m spatial resolution by applying the same inundation model developed by Li et al. (2013) and the SRTM 30-m DEM data.

To evaluate the flood mapping methodology presented in this study, we used corresponding datasets in the form of storm-tide site and high-water-mark data and the FEMA 3-m-resolution Hurricane Sandy SSF products. Our assessment shows high consistency between our ATMS-derived 30-m flood maps and the validation data. Specifically, 88% of the storm-tide and high-water-mark sites were located within the ATMS-mapped flood area. There was also a good agreement between ATMS- and FEMA flooded areas, with an accuracy of 88% and a correlation of 0.94. When evaluated against round level observation from social-media flood reports, 95% of the flickr flood reports were similarly contained within our flood map. The remaining errors may be attributed to the soil moisture variations before and after the hurricane. Overall, the proposed methodology was able to produce high-quality and high-resolution flood map over large scale coastal areas.

Passive microwave observation is found useful and practical for storm-surge flood estimations, particularly for rainy and cloudy weather. Nevertheless, some key discussions that result from our study are as follows: 1) Because of the limited spatial resolution of the ATMS data, pure land or water pixels were very difficult to identify. Accordingly, prior knowledge of land samples and water samples based on land cover and river density can improve end-member accuracy. 2) Although we re-sampled the ATMS-derived flood map and FEMA SSF products to the same resolution for comparison, the spatial resolution differences of the various datasets may result in some inconsistencies or errors. 3) In our study, the ATMS data with small satellite zenith angles and daylight orbits were used for the flood estimation. A logical extension of this work would be to study the extent to which the satellite zenith angle and azimuth angle, solar zenith angle and azimuth angle affect the passive microwave signal. 4) Although passive microwave data can penetrate clouds, the resulting data, particularly from higher frequency channels, are still affected by precipitating clouds. Eliminating the effects of such clouds is another future research direction that emerges from this work. 5) The pixels' soil moisture conditions may be different before and after flooding. The extent to which the soil moisture difference between pre- and post-flooding affects the water fraction difference may also need further investigations in the future. 6) It also needs a note that this approach may only be applied to large scale floods, as we performed many tests, the methodology may not work well for small scale floods.

Acknowledgments

The work is supported by NOAA JPSS Program Office under grant #NA12NES4400008 and by NASA Disaster Program under grant #NNX12AQ74G. The manuscript's contents are solely the opinions of the authors and do not constitute a statement of policy, decision, or position on behalf of NOAA or NASA or the U. S. Government. We appreciate the helpful and constructive comments from the reviewers!

References

Bates, P. D., Wilson, M. D., Horritt, M. S., Mason, D. C., Holden, N. and Currie, A., 2006. Reach scale floodplain inundation dynamics observed using airborne synthetic aperture radar imagery: Data analysis and modeling. *Journal of Hydrology*, 328, 306-318.

Carroll, M.L., Townshend, J.R., DiMiceli, C.M., Noojipady, P., and R. and Sohlberg, A., 2009: A new global raster water mask at 250 m resolution. *International Journal of Digital Earth*, 2 (4), 291-308.

Cho, K., and Nishiura, K., 2010. A study on cloud effect reduction for extracting sea ice area from passive microwave sensor data. *In Proc. International Archives of the Photogrammetry, Remote Sensing and Spatial Information Science,* XXXVIII, 1042-1045.

Choudhury, B. J., 1989. Monitoring global land surface using Nimbus-7 37 GHz data - Theory and examples. *International Journal of Remote Sensing*, 10 (10), 1579-1605.

Ferraro, R. R., Smith, E.A., Berg, W., and Huffman, G.J., 1998. A screening methodology for passive microwave precipitation retrieval algorithms. *Journal of Atmospheric Sci*ence, 55 (9), 1583-1600.

Li, S., Sun, D. L., Yu, Y., Csiszar, I., Stefanidis, A., and Goldberg, M. D., 2012a. A New Shortwave Infrared (SWIR) Method for Quantitative Water Fraction Derivation and Evaluation with EOS/MODIS and Landsat/TM data. *IEEE Transactions on Geoscience and Remote Sensing*, 51 (3), 1852-1862.

Li, S., Sun, D.L., and Yu, Y., 2013b. Automatic Cloud Shadow Removal from Flood/Standing Water Maps using MSG/SEVIRI Imagery. *International Journal Remote Sens*ing, 34(15), 5487-5502.

Li, S., Sun, D. L., Goldberg, M. D., and Stefanidis, A., 2013c. Derivation of 30-m-resolution water maps from TERRA/MODIS and SRTM. *Remote Sensing of Environ*ment, 134, 417-430.

Jin, Y. Q., 1999. Flooding index and its regional threshold value for monitoring floods in China from SSM/I data. *International Journal of Remote Sensing*, 20 (5), 1025-1030.

Sippel, S. J., Hamilton, S. K., Melack, J. M., and Choudhury, B. J., 1994. Determination of inundation area in the Amazon river floodplain using the SMMR 37 GHz polarization difference. *Remote Sensing of Environ*ment, 48 (1), 70–76.

Sippel, S. J., Hamilton, S. K., Melack, J. M., and Novo, E. M. M., 1998. Passive microwave observations of inundation area and area/stage relation in the Amazon River floodplain. *International Journal of Remote Sensing*, 19 (16), 3055– 3074.

Sheng, Y., Gong, P., and Q., Xiao, 2001. Quantitative dynamic flood monitoring with NOAA AVHRR. *International Journal of remote sensing*, 22 (9), 1709–1724.

Sun, D. L., Yu, Y. Y., and Goldberg, M.D., 2011. Deriving water fraction and flood maps from MODIS images using a decision tree approach. *IEEE Journal of Selected Topics in Applied Earth Observation and Remote Sens*ing, 4 (4), 814-825.

Sun, D. L., Yu, Y. Y., Zhang, R., Li, S., and Goldberg, M.D., 2012. Towards operational automatic flood detection using EOS/MODIS data. *Photogrammetric Engineering of Remote Sens*ing, 78 (6), 637-646.

Tanaka, M., Sugimura, T., Tanaka, S., and Tamai, N., 2003. Flood drought cycle of Tonle Sap and Mekong Delta area observed by DMSP-SSM/I. *International Journal of Remote Sensing*, 24 (7), 1487–1504.

Weng, F., Yang, H., and Zou, X., 2013. On Convertibility from antenna to sensor brightness temperature for ATMS. *IEEE Geophysical Research Lett*ers, 10 (4), 771-775.

Zheng, W., Liu, C., Wang, Z. X, and Xin, Z. B., 2008. Flood and waterlogging monitoring over

Huaihe River Basin by AMSR-E data analysis. *China Geographic Science*, 18 (3), 262-267.

List of Tables

Table 1. NPP/VIIRS Imager multi-spectral channels used to observe surface water

Band No.	Central Wavelength (µm)	Wavelength Range (µm)	Horizontal Sample Interval (km)
I1	**0.640**	**0.600 - 0.680**	**0.371 x 0.387**
I2	**0.865**	**0.846 – 0.885**	**0.371 x 0.387**
I3	**1.61**	**1.580 – 1.640**	**0.371 x 0.387**
I5	**11.45**	**10.500 – 12.400**	**0.371 x 0.387**

Table 2. Characteristics of ATMS channels used to observe earth surface

Cannel	Center frequency (GHz)	Beam width $(^{o})$	Quasi polarization	Characterization at nadir
1	23.80	5.2	QV	Surface
2	31.40	5.2	QV	Surface
3	50.30	2.2	QH	Surface
4	51.76	2.2	QH	Surface
16	88.20	2.2	QV	Surface

List of Figures

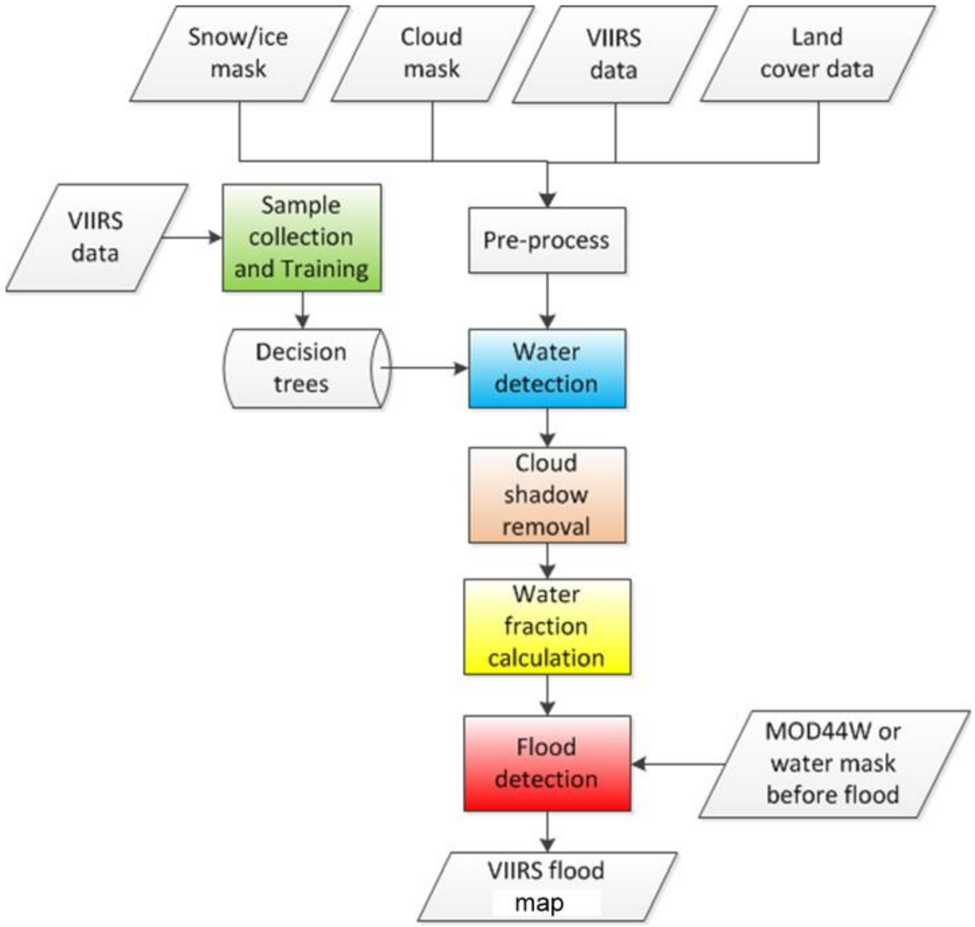

Figure 1. Flow chart for deriving flood from VIIRS data

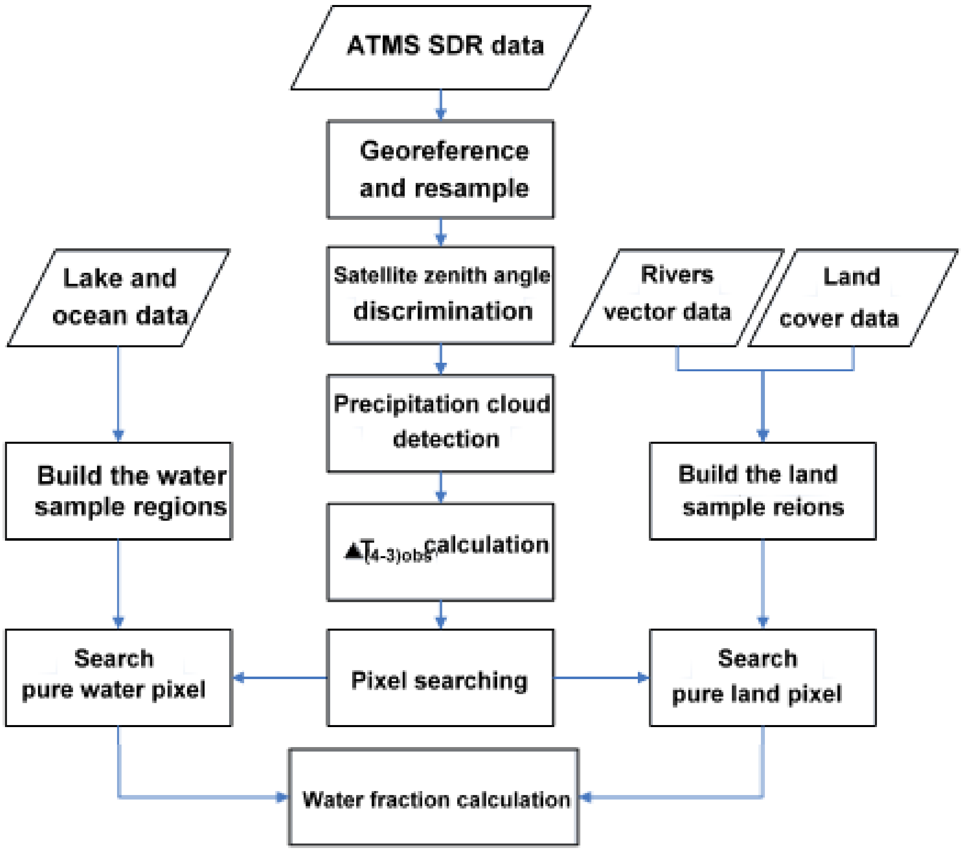

Figure 2. Flowchart of water fraction estimation from ATMS data.

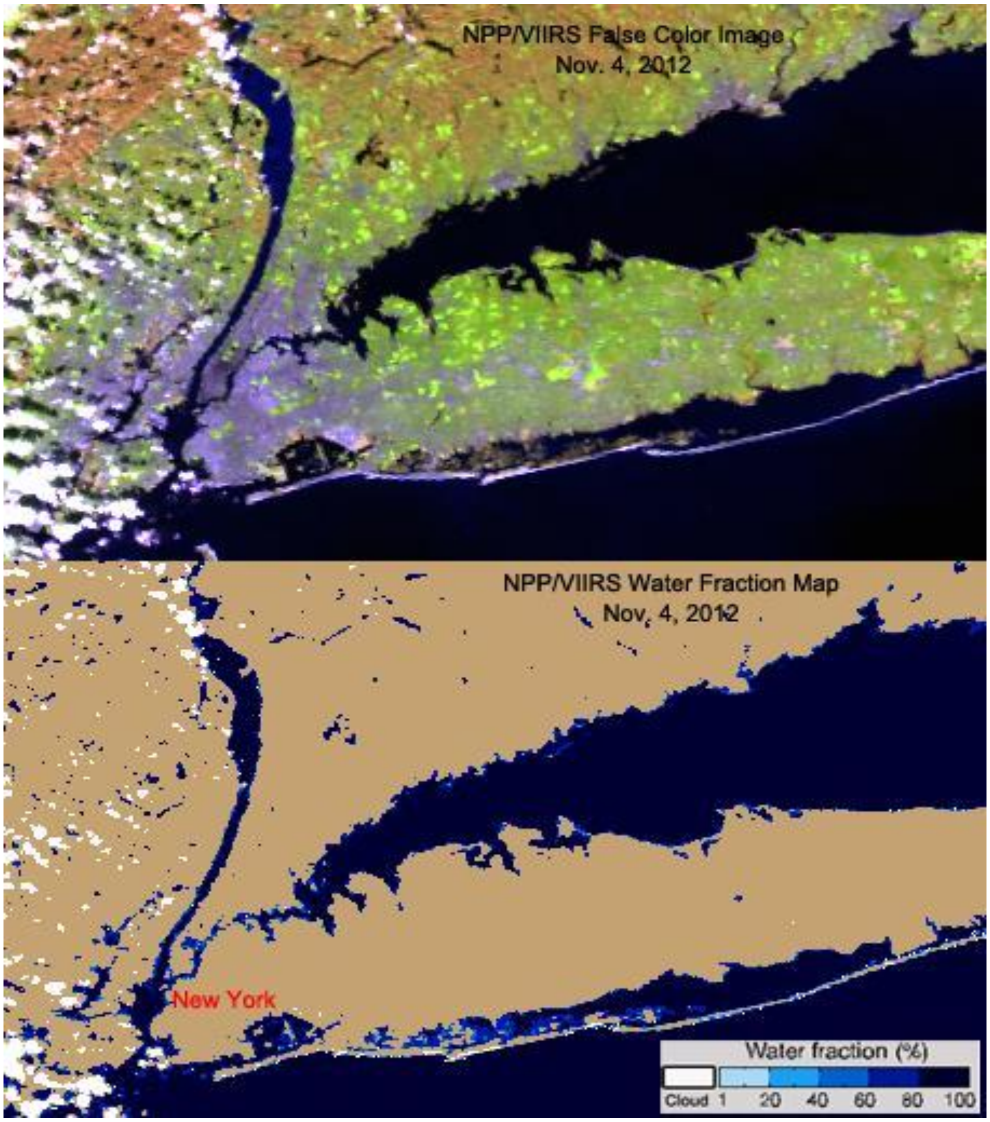

Figure 3. (Upper) VIIRS false-color image (VIIRS 3, 2, 1) at 17:17 (GMT) on Nov. 04, 2012. Dark blue and black correspond to water bodies. (Lower) VIIRS-derived water fraction for the same period using the Li et al. (2013a) algorithm**.**

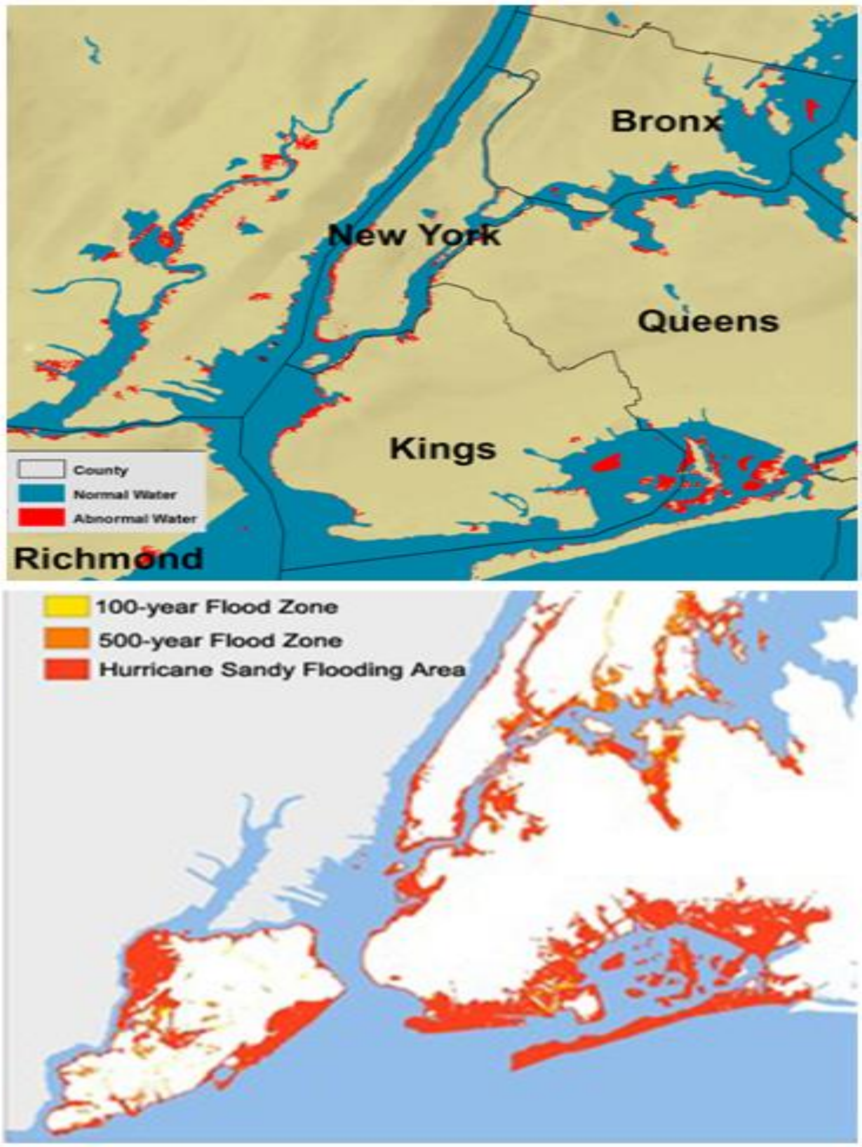

Figure 4. Flood map at 30-m resolution derived from VIIRS and SRTM in the New York metropolitan area on Nov. 04, 2012 (Upper) compared with a flooding area map from FEMA over parts of lower Manhattan, the Upper East Side, Red Hook, and Greenpoint (Lower).

.

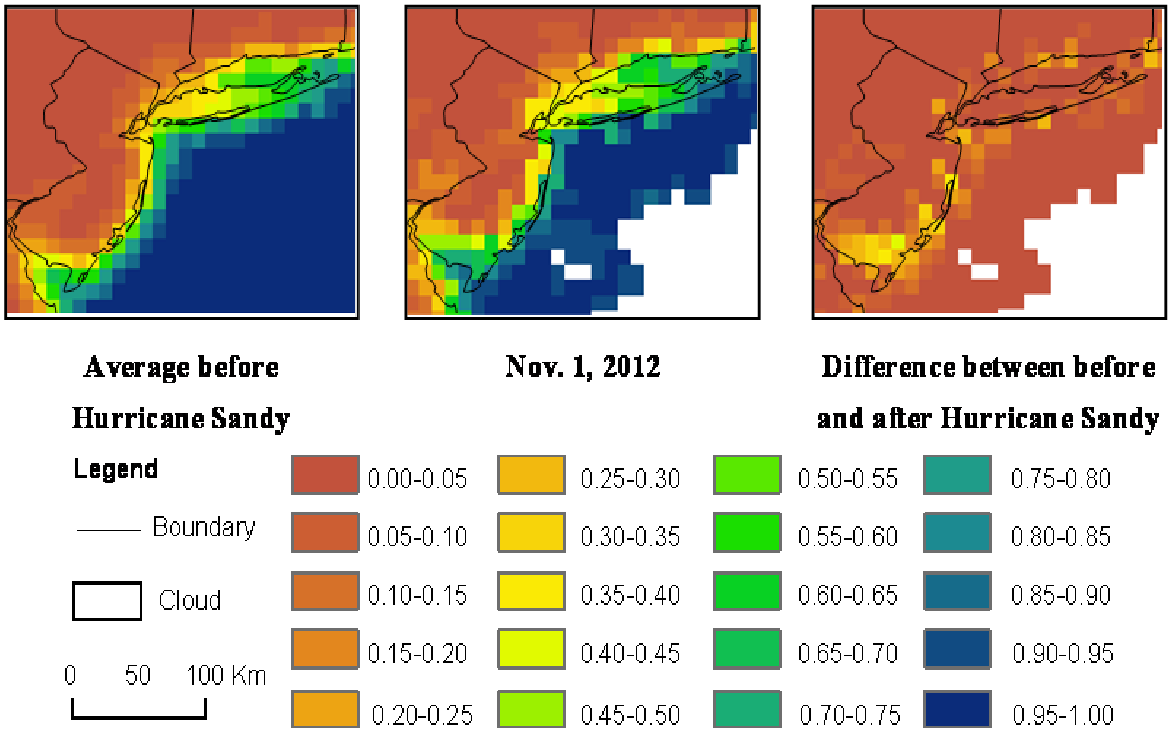

Figure 5. Water fraction maps before (left) and after (middle) Hurricane Sandy and their difference map (right)

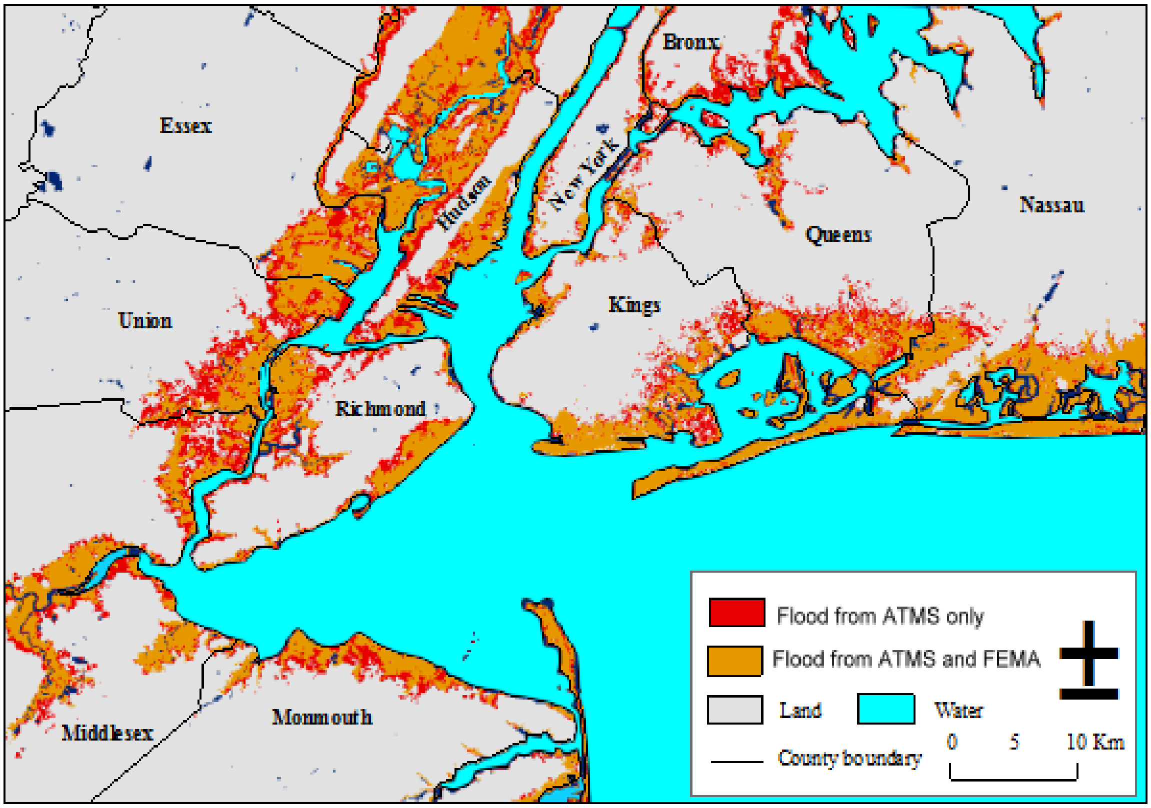

Figure 6. 30-meter resolution flood map generated from the ATMS and DEM on Nov. 1st, 2012, overlapped and compared with the FEMA SSF flood product.

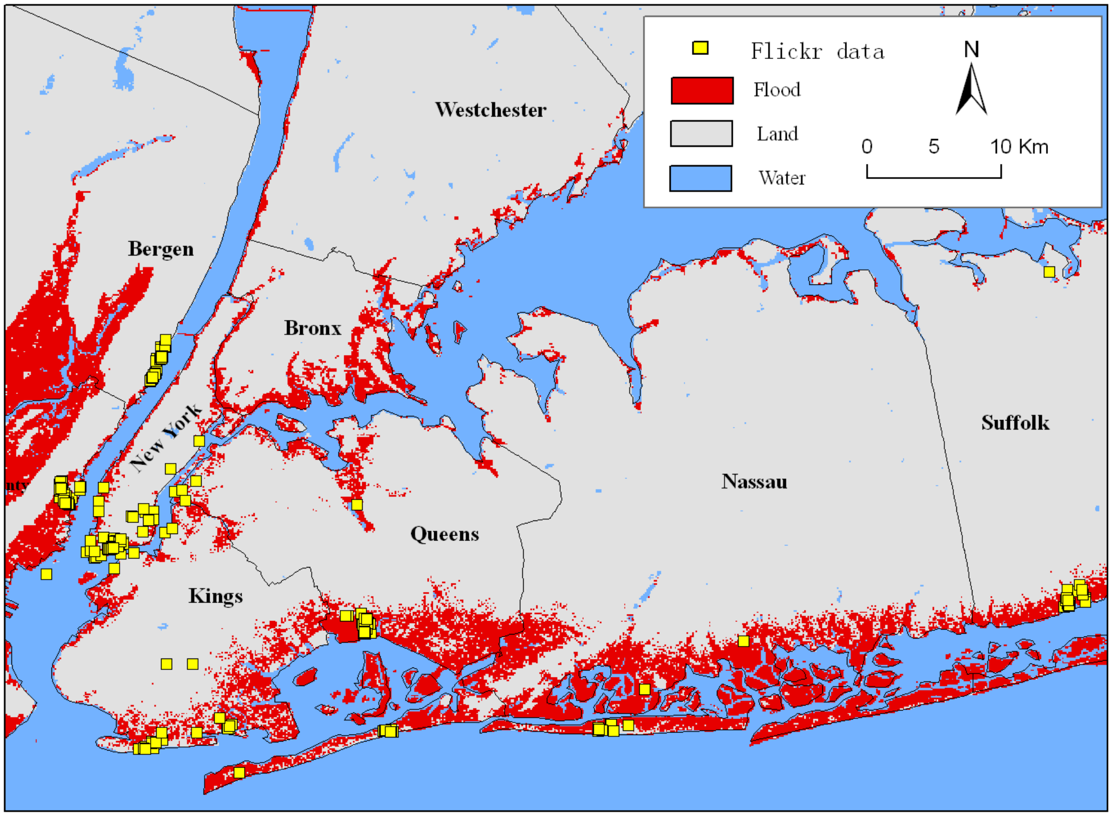

Figiure 7. Flickr images reporting flooding (yellow dots) overlaid on the ATMS-derived flood map in the vicinity of New York City and its boroughs.